A&A 509, A19 (2010)
DOI: 10.1051/0004-6361/200809686

Astronomy & Astrophysics

The molecular gas content of the advanced S+E merger NGC 4441

Evidence for an extended decoupled nuclear disc?

E. Jütte[1,2], S. Aalto[3], and S. Hüttemeister[1]

[1] Astronomisches Institut der Ruhr-Universität Bochum, 44780 Bochum, Germany
e-mail: eva.juette@astro.rub.de
[2] Astron, 7990AA Dwingeloo, The Netherlands
[3] Onsala Space Observatory, Chalmers University of Technology, 439 92 Onsala, Sweden

Received 29 February 2008 / Accepted 28 August 2009

ABSTRACT

Context. Despite their importance to galaxy evolution, mergers between a spiral and an elliptical (S+E mergers) have been poorly studied so far. NGC 4441 is a nearby candidate of an advanced remnant of such a merger, showing typical tidal structures such as an optical tail and two shells as well as two H I tails.
Aims. Studying the molecular gas content provides clues about the impact of a recent merger event on the star formation. Simulations of S+E mergers yield conflicting predictions about both the strength and the extent of an induced starburst. Thus, observations of the amount and the distribution of the molecular gas, the raw material of star formation, are needed to understand the influence of the merger on the star formation history.
Methods. ^{12}CO and ^{13}CO (1−0) and (2−1) observations were obtained using the Onsala Space Observatory 20 m and IRAM 30 m telescope as well as the Plateau de Bure interferometer. These data allow us to carry out a basic analysis of the molecular gas properties, such as estimates of the molecular gas mass, temperature, and density and the star formation efficiency.
Results. The CO observations detect an extended molecular gas reservoir out to ∼4 kpc, with a total molecular gas mass of $\sim 5 \times 10^8\ M_\odot$. Furthermore, high resolution imaging shows a central molecular gas feature, which is probably a rotating disc hosting most of the molecular gas ($\sim 4 \times 10^8\ M_\odot$). This nuclear disc has a different sense of rotation to the large-scale H I structure, indicating a kinematically decoupled core. We modeled the state of the interstellar medium with the radiative transfer code RADEX, using the ratios of the ^{12}CO to ^{13}CO line strenghts. The results are consistent with a diffuse ($n \leq 10^3$ cm^{-3}) molecular medium with no significant indications of cold, dense cores of ongoing star formation. This is in agreement with the moderate star formation rate of 1−2 $M_\odot$ yr^{-1} measured for NGC 4441. Assuming a constant star formation rate, the gas depletion time is $\tau = 4.8 \times 10^8$ yr. NGC 4441 might be a nearby candidate early-type galaxy with a dominant A-star population, a so-called E+A galaxy, which is in a post-starburst phase several 10^8 yr after a merger event.

Key words. galaxies: interactions – galaxies: starburst – galaxies: individual: NGC 4441 – radio lines: galaxies – radio lines: ISM

1. Introduction

Following the ΛCDM models for galaxy evolution, mergers between galaxies occur frequently and are essential for forming the large galaxies that we see today (e.g., Steinmetz 2003). While most observational studies concentrate on mergers between two spiral galaxies, simulations by Naab & Burkert (2000), Naab & Burkert (2001), Khochfar & Burkert (2003), and Naab et al. (2006) demonstrated the importance of mergers between a spiral and an elliptical (so-called S+E mergers) to the formation of bright ellipticals. Observations of this class of mergers are needed to investigate their relevance and influence on galaxy evolution.

The well studied major mergers of two gas-rich disc galaxies can lead to ultraluminous infrared galaxies (ULIRGs, $L_{\rm FIR} > 10^{12}\ L_\odot$, Sanders & Mirabel 1996) because of a merger-induced extreme starburst. However, S+E mergers have been poorly studied so far and thus, it is unclear whether starbursts generally occur in these mergers and how they evolve. Besides the lack of observations, models of S+E mergers are in strong disagreement with the predictions of interaction-triggered enhanced star formation. Weil & Hernquist (1993) predict that a congregation of gas forms in the centre of the remnant galaxy, leading to a strong gas concentration and thus resulting in a starburst, similar to ULIRGs but less intense. Simulations by Kojima & Noguchi (1997), however, predict dispersed gas clouds that might not produce a starburst at all, because the density of the gas is too low for it to collapse and form new stars. To understand galaxy evolution, it is necessary to know which scenario is more realistic and in particular how S+E mergers influence the stellar population content of the remnant. Observations of the molecular gas can show the amount and extent of the raw material available for star formation. Investigations of the molecular gas content in interacting galaxies showed a concentration of gas towards the centre and higher gas mass compared to non-interacting galaxies (e.g., Braine & Combes 1992, 1993; Horellou & Booth 1997). In ULIRGs, the molecular gas forms compact nuclear rotating rings and discs, fueling the central starburst (e.g., Bryant & Scoville 1996; Downes & Solomon 1998; Bryant & Scoville 1999; Greve et al. 2009). It is not known whether this is also the case in S+E mergers.

One "prototypical" S+E merger candidate is NGC 4194, the Medusa. In the optical, we see a diffuse tail going to the north and on the opposite side two stellar shells are visible, consistent

Table 1. Basic properties of NGC 4441.

Property	
RA (2000)	12:27:20.3
Dec (2000)	+64:48:05
$v_{\rm opt,hel}$ (km s^{-1})	2722
D (Mpc)	36
type[a]	SAB0+ pec
$L_{\rm B}$ (10^9 $L_\odot$)	10.1
$L_{\rm FIR}$ (10^9 $L_\odot$)	5.4
$SFR_{\rm FIR}$ ($M_\odot$)	1.0
$SFR^b_{\rm 20\ cm}$ ($M_\odot$)	2.4
1′	10.5 kpc

The distance is based on H_0 = 75 km s^{-1} Mpc^{-1}. [a] The Hubble type is taken from de Vaucouleurs et al. (1995); [b] taken from Manthey et al. (2008a).

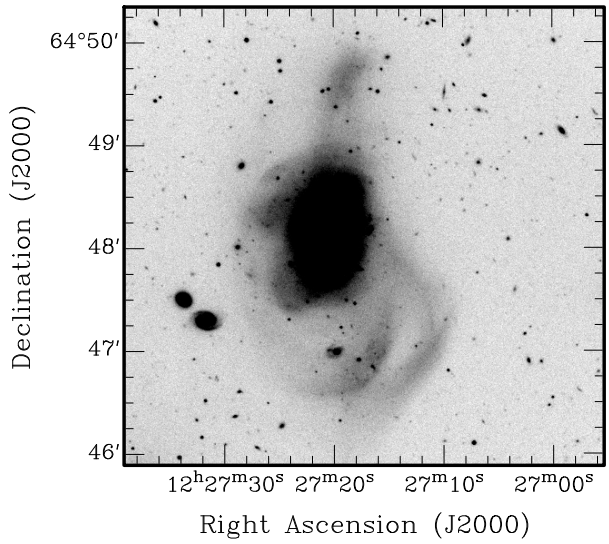

Fig. 1. *R*-Band image of NGC 4441, observed with the Calar Alto 2.2 m, integration time 1 h (Jütte et al. 2009, in prep.). Note the tidal tail to the north and two stellar shells to the south-west. The two galaxies south-east of the main body are background galaxies.

with predictions. Molecular gas is found out to 4.7 kpc away from the centre, i.e., much more spread out than in the case of a ULIRG (Aalto & Hüttemeister 2000; Aalto et al. 2001). However, this galaxy is clearly undergoing an intense starburst phase, albeit not as intense as in ULIRGs (Weistrop et al. 2004).

Here we present CO maps of another S+E merger candidate, NGC 4441 (see Table 1) (see discussion of merger history in Manthey et al. 2008a). The optical morphology of this galaxy is very similar to that of the Medusa. It possesses one tidal tail and two bright shells on the opposite side, which is typical for S+E merger remnants (e.g., Quinn 1984; Dupraz & Combes 1985; Kojima & Noguchi 1997). The main body has an elliptical shape (Bergvall 1981) with a small dust lane through the centre along the minor axis. In contrast to the strong similarities between its optical morphology and that of the Medusa, the atomic gas distribution differs significantly, since the H I forms two symmetric tidal tails (compared to only one tail in the Medusa, Manthey et al. 2008b). In NGC 4441, the total H I mass is 1.5 × 10^9 $L_\odot$ (Manthey et al. 2008a). The ongoing star formation rate is rather low (1−2 $M_\odot$ yr^{-1}), because the merger is in such an advanced phase that most of the gas has been already used for star formation (Manthey et al. 2005, 2008a). Using optical spectra, Bergvall (1981) found indications of a period of enhanced star formation in the past, since the stellar population is younger than that of a normal elliptical galaxy. Our own optical spectra confirm this and we estimate that a moderate starburst occurred ∼1 Gyr ago (Manthey et al. 2005).

2. Observations and data reduction

2.1. Onsala Space Observatory 20 m

First ^{12}CO(1−0) observations were carried out in March 2003 using the 20 m telescope of the Onsala Space Observatory (OSO), Sweden. CO observations were completed with a SIS-mixer and a correlator with a total bandwidth of 512 MHz. The main beam efficiency at 115 GHz was η = 0.43. To account for the highly variable sky background, the observations were done in beam switching mode. The switching frequency was 1.8 Hz and the beam throw 11′. We observed the centre position as given in Table 1 in good weather conditions, i.e., 30% humidity and clear, stable sky. The pointing and focus was regularly checked during observations with the calibration sources R Leo and R Cas. Table 2 summarises the observations.

Table 2. Parameters for the CO observations of NGC 4441 with the OSO 20 m and IRAM 30 m telescopes as well as the Plateau de Bure interferometer.

obs. parameters	IRAM 30 m	OSO 20 m	PdB
$T_{\rm sys}$ (K)	200−340 (^{12}CO)	∼350	180
	∼145 (^{13}CO)	–	–
$\theta_{\rm beam}$ CO(1–0)	22″	33″	3.25″
$\theta_{\rm beam}$ CO(2–1)	11″	–	–
Δv CO(1–0)	21.0 km s^{-1}	33.8 km s^{-1}	6.6
Δv CO(2–1)	21.0 km s^{-1}	–	–
η	0.75 (1–0) / 0.52 (2–1)	0.43	0.6–0.9

The velocity resolution given is a smoothed one, which is used throughout this paper.

2.2. IRAM 30 m

Follow-up CO observations of NGC 4441 were done with the IRAM 30 m telescope on Pico Veleta, Spain in July 2004. The weather conditions were good. We mapped an extended CO distribution both in the ^{12}CO(1−0) and (2−1) line. We used the A 100 and B 100 as well as the A 230 and B 230 receivers to observe the ^{12}CO(1−0) and (2−1) lines simultaneously. The 1 MHz filterbank with 2 × 512 channels was chosen as a backend. The observations were done in beam switching mode. Pointing and focus calibration were regularly checked by observing Saturn. As a second pointing source near NGC 4441, we observed the calibration source 0954+658. To achieve a proper spatial coverage (a fully sampled map) even in the ^{12}CO(2−1) line, we mapped the centre using a 3 × 3 grid with a spacing of 6″, i.e., half the width of the ^{12}CO(2−1) beam. For the outer positions, we used steps of 22″ (full ^{12}CO(1−0) beamwidth) to cover a larger area, since we wished to track the extent of the molecular gas. In total, we observed 17 positions out to 44″. In the most distant pointings, we do not find emission. Thus, we concluded that we had covered the central molecular gas extent completely and were able to estimate source size and total mass.

The central position was also observed in ^{13}CO and the (1−0) and (2−1) transitions were measured simultaneously.

2.3. Plateau de Bure

To map the CO distribution at higher spatial resolution, we obtained interferometric observations in December 2005, May and July 2007 using the Plateau de Bure interferometer (PdBI). The observations were completed with a dual polarization receiver covering a bandwidth of 4 GHz with 240 channels, centred on the redshifted CO(1−0) line at 114.252 GHz. This leads to a resolution of 6.56 km s^{-1}. The beamsize was 3.25″ × 2.65″, and the position angle 122°. The primary beam at 115 GHz was 45″. In total, we had an integration time of 16 h on source The observations were done with the 6Cq−E10, 5Dq−W05, and 5Dq configurations. The flux, phase, and bandpass calibrators were 1044+719, 0418+380, 3C 273, and 3C 454.

2.4. Data reduction

The CLASS[1] package was used for the data reduction at Onsala; the IRAM CO data were reduced using XS[2], a graphical reduction and analysis software for mm spectral line data written by Bergman. After checking the quality of each single spectrum, the data were averaged with a weighting based on the system temperature and integration time. A first-order baseline was fitted to the resulting spectrum and subtracted. The data were converted to main-beam brightness temperature ($T_{\rm MB}$) using the beam efficiencies given in Table 2. Finally, we smoothed the spectra to a velocity resolution of 21 km s^{-1} (IRAM) and 34 km s^{-1} (OSO), respectively, to achieve a higher signal-to-noise ratio in individual channels. For the different positions in the ^{12}CO(1−0) map, we reached a noise level of 1.6–5.3 mK; in the ^{12}CO(2−1) map, the noise level lies between 2.1 and 9.6 mK $T_{\rm MB}$. For ^{13}CO, noise levels are 0.7 mK (1−0) and 1.3 mK (2−1).

The Plateau de Bure data were reduced using the GILDAS task CLIC. After flagging and phase and flux calibration using the observed calibrator sources, a uv-table of the science data was created. The uv-table was then transformed into a map using a natural weighting scheme. This dirty map was CLEANed to correct for sidelobes. After CLEANing, the rms noise level in the cube was 2.9 mJy beam^{-1}. Finally, moment maps were created from the CLEANed cubes using a clip value of $4\sigma = 0.012$ Jy beam^{-1}.

3. Results

3.1. CO distribution and molecular mass

Our first set of OSO observations inferred a molecular gas content in the inner 33″ of ∼4.7 × 10^8 $M_\odot$. The mass was derived by calculating the H_2 column density

$$N(\mathrm{H_2}) = X_{\rm CO} \times \int I_{\rm CO} \mathrm{d}v \ \mathrm{cm^{-2}} \quad (1)$$

and thus

$$M_{\rm H2} = N(\mathrm{H_2}) \times m(\mathrm{H_2}) \times \Omega \ M_\odot, \quad (2)$$

where $X_{\rm CO}$ is the CO-H_2 conversion factor, $I_{\rm CO}$ the intensity of the CO line in Kelvin, $m(H_2)$ the mass of an H_2 molecule in kg, and Ω the area covered by the beam in linear scales (cm^2). We used a "standard" conversion factor of $X_{\rm CO} = 2.3 \times 10^{20}$ cm^{-2} (K km s^{-1})$^{-1}$, with reference to Strong et al. (1988). Figure 2 shows the observed CO spectrum.

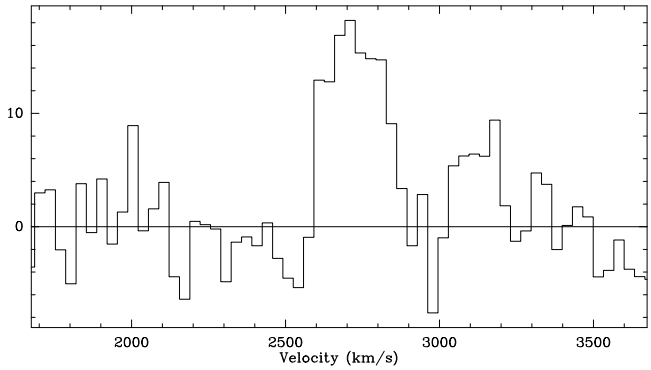

Fig. 2. ^{12}CO(1−0) spectrum observed with the OSO 20 m telescope. The intensity is given in $T_{\rm MB}$ (mK).

Mapping NGC 4441 in CO with the IRAM 30 m telescope, we found a molecular gas distribution that was extended in particular to the south-east. Table 3 gives the pointings relative to the centre position, the noise levels, the widths determined from Gaussians of both the ^{12}CO(1−0) and CO(2−1) lines, and the integrated intensities. In Figs. 3 and 4, we present the spectra of the mapped positions for both the ^{12}CO(1−0) and CO(2−1) lines.

Based on the assumption of a Gaussian distribution for the intensity, we plotted the intensity versus radial distance from the centre, and fitted a Gaussian to derive the source size (see Fig. 5 for ^{12}CO(1−0)). The true source $\Theta_{\rm source}$ size can be estimated from both the observed source size $\Theta_{\rm obs}$ and the known beam size $\Theta_{\rm beam}$ by assuming that $\Theta^2_{\rm source} = \Theta^2_{\rm obs} - \Theta^2_{\rm beam}$. We derive a deconvolved source size of $FWHM$[3] = 22″ ± 1″ (3.9 kpc) for ^{12}CO(1−0). The estimated source size for ^{12}CO(2−1) is slightly larger (30″ ± 3″), but this is probably an artefact of the undersampling of the source coverage and lower signal-to-noise ratios of data for this transition. In our discussion below, we assume that ^{12}CO(2−1) and (1−0) have identical extents. We determined a central H_2 column density of 1.8 × 10^{21} cm^{-2} and calculated a total molecular gas mass of 4.6 × 10^8 $M_\odot$, by applying Eqs. (1) and (2).

Since we found extended gas to the south and east (see Figs. 3 and 4) but only tentative detections to the north and west, the source seems to be asymmetric. However, the estimated mass is in good agreement with the total mass derived from the OSO observations, which due to the larger beam cover the whole area of CO emission.

3.2. Molecular gas kinematics

The spectra in both maps (Figs. 7, 3, 4) clearly show two components, a fainter one (measured at the centre) at $v_{\rm lsr}$ = 2690 ± 15 km s^{-1} (2660 ± 18 km s^{-1} in ^{12}CO(2−1)) and a more dominant one at $v_{\rm lsr}$ = 2790 ± 10 km s^{-1}. Comparing the spectra at individual positions, the relative intensities of both line components change, in particular in the SE direction. In the ^{12}CO(2−1) map, the more blueshifted line is the brighter one at the offset position (+15.6″, −15.6″) (see Fig. 4). This component is centred on 2660 km s^{-1} in ^{12}CO(2−1) at each position, whereas in ^{12}CO(1−0) there seems to be a slight shift from 2690 km s^{-1} at the centre to 2660 km s^{-1} in the outer region.

[1] Continuum and Line Analysis Single-dish Software, http://www.iram.fr/IRAMFR/GILDAS/

[2] ftp://yggdrasil.oso.chalmers.se/pub/xs/

[3] Full width of half maximum.

Table 3. CO line parameters of the map of NGC 4441.

Δ RA (″)	Δ Dec (″)	$\mathrm{rms}_{\mathrm{CO(1-0)}}$ (mK)	$\Delta v_{\mathrm{CO(1-0)}}$ (km s^{-1})	$I_{\mathrm{CO(1-0)}}$ (K km s^{-1})	$\mathrm{rms}_{\mathrm{CO(2-1)}}$ (mK)	$\Delta v_{\mathrm{CO(2-1)}}$ (km s^{-1})	$I_{\mathrm{CO(2-1)}}$ (K km s^{-1})
0	0	2.50	292	7.52	7.67	324	6.10
6	6	4.62	283	2.34	6.72	240	1.84
0	6	3.43	328	4.80	6.34	270	3.51
–6	6	5.33	209	2.68	5.95	252	2.69
6	0	3.78	267	4.24	7.67	302	3.64
–6	0	3.86	336	1.69	7.67	247	2.50
6	–6	5.28	344	6.65	7.87	220	6.34
0	–6	3.75	320	4.60	9.6	285	6.14
–6	–6	4.42	259	3.70	9.6	308	3.97
0	22	2.19	220	0.92	3.62	–	–
–22	0	2.06	–	1.67	2.88	–	–
0	–22	1.64	262	1.44	3.07	–	–
22	0	2.33	316	2.47	2.30	275	0.88
15.6	–15.6	2.39	310	2.53	2.11	318	2.23
44	0	1.77	–	–	3.07	–	–
0	–44	2.18	–	–	2.11	–	–
31	–31	2.00	–	–	2.88	–	–

The reference coordinates are the centre coordinates (J2000): RA: $12^{\mathrm{h}}27^{\mathrm{m}}20.36^{\mathrm{s}}$, Dec: +64°48′06″. Given are the offset positions, the total velocity range of the CO(1−0) and CO(2−1) line and the intensities of both lines. The temperatures are measured in T_{MB}.

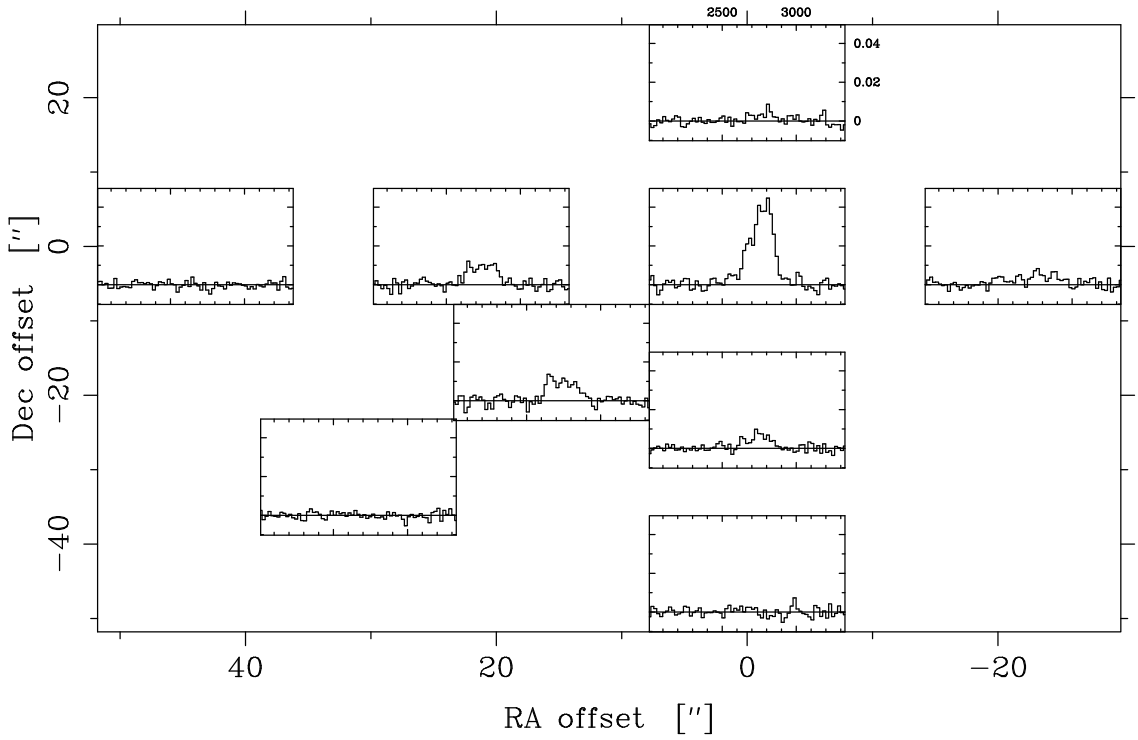

Fig. 3. Large ^{12}CO(1−0) map of NGC 4441, observed with the IRAM 30 m telescope. The outer tick marks denote the spacing of the observed positions, and the inner tick marks represent the velocity (km s^{-1}) and T_{MB} (mK), respectively.

Generally, the single dish molecular gas kinematics agrees with the overall central kinematics of the H I presented in Manthey et al. (2008a) in terms of the covered velocity range.

3.3. The nuclear region

In Fig. 8, the integrated interferometer CO(1−0) intensity and velocity field maps of NGC 4441 are shown. Since interferometers filter out emission from extended diffuse gas, the maps show the distribution of fairly dense CO. We found what appears to be a small, inclined, nuclear disc aligned with the dust lane seen in the optical. The position angle of both the dust lane and the disc are identical. The orientation of the disc is northeast-southwest. Thus, it is inclined with respect to the optical major axis. Most of the gas is concentrated around the optical nucleus. A second, fainter component of low velocity dispersion is found north-east of the centre seen in Figs. 8 and 6 ("hook" in Fig. 9). This second peak is aligned with a broadened dust feature seen in the optical image (Fig. 10).

We note that besides the central dust lane associated with the bulk of the molecular gas, there are several faint off-centre dust lanes visible in optical images (e.g., south of the centre, Fig. 10).

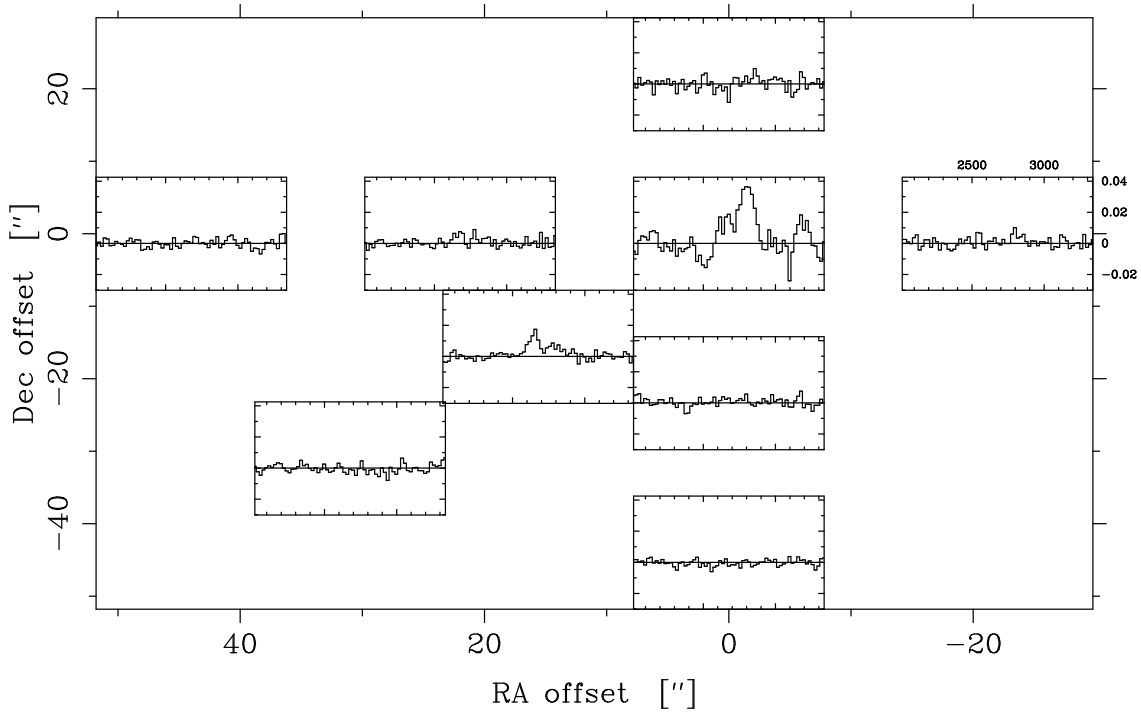

Fig. 4. Large ^{12}CO(2−1) map of NGC 4441, observed with the IRAM 30 m telescope. The outer tick marks denote the spacing of the observed positions, and the inner tick marks represent the velocity (km s^{-1}) and $T_{\rm MB}$ (mK), respectively.

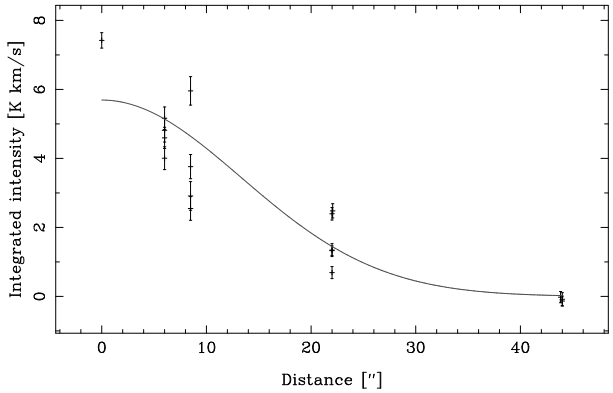

Fig. 5. The observed integrated intensities of ^{12}CO(1−0) are plotted versus the distance from the central position. To estimate the molecular source size we fitted a Gaussian and determined the $FWHM = 22 \pm 1''$.

Table 4. Properties of the nuclear molecular gas feature found in NGC 4441.

Property	Value
size ($''$/kpc)	$10.3 \times 6.4/1.8 \times 1.1$
PA (°)	222
Δv (km s^{-1})	295
$F_{\rm CO}$ (Jy km s^{-1})	29.1
$M_{\rm disc,H2}$ ($M_\odot$)	4.1×10^8
$M_{\rm disc,dyn}$ ($M_\odot$)	2.1×10^9

These lanes were within the primary beam of the PdBI. Thus, if significant molecular gas were also associated with these dust lanes, we would have detected it.

The total gas mass of the disc was calculated to be $M_{\rm H2} = 0.92 \times 10^4 \times F_{\rm CO} \times D^2 = 4.1 \times 10^8\ M_\odot$, where D denotes the distance in Mpc, F being the integrated CO flux in Jy km s^{-1}. Thus, with the interferometric observations we detected ∼87% of the molecular gas mass seen in single-dish observations.

If we interpret the central feature as an inclined disc, its position-velocity diagram can be interpreted as the regular rotation pattern of a solid body (Figs. 8, 9). The main parameters of this feature are given in Table 4. We calculated the dynamical mass of the nuclear disc with $v_{\rm rot,max} = 100$ km s^{-1} at a radius of $R = 5'' = 875$ kpc. The disc appears to be close to edge-on, so we assume an inclination of $i = 80°$. An error of ±10° in inclination does not affect our result significantly. Thus, we calculate the dynamical mass to be $M_{\rm dyn}(M_\odot) = R \times (v_{\rm rot,max}/\sin i)^2\ G^{-1} = 2.1 \times 10^9\ M_\odot$.

3.4. ^{13}CO(1–0) and ^{13}CO(2–1)

We also observed the centre position of NGC 4441 in ^{13}CO(1−0) and ^{13}CO(2−1). The ^{13}CO(1−0) line is clearly detected, the ^{13}CO(2−1) is only tentatively detected at a 3σ level, but a feature at the expected velocity of 2790 km s^{-1} is found (see Fig. 11). Table 5 gives the linewidths and integrated intensities of all four lines at the centre position. We fitted only one single Gaussian to the ^{13}CO lines. The fitted centre velocity of ^{13}CO(1−0) (Table 5) is in-between the derived values for the blue- and red-shifted line using the ^{12}CO transitions. In contrast, in ^{13}CO(2−1) we see (if at all) the component of higher velocity, which is also the strongest, in ^{12}CO at the centre. However, the signal-to-noise ratio of the ^{13}CO(2−1) line is too low to draw firm conclusions.

In Table 6, the derived molecular gas mass and the molecular line intensity ratios based on the integrated intensities given in Table 5 are listed.

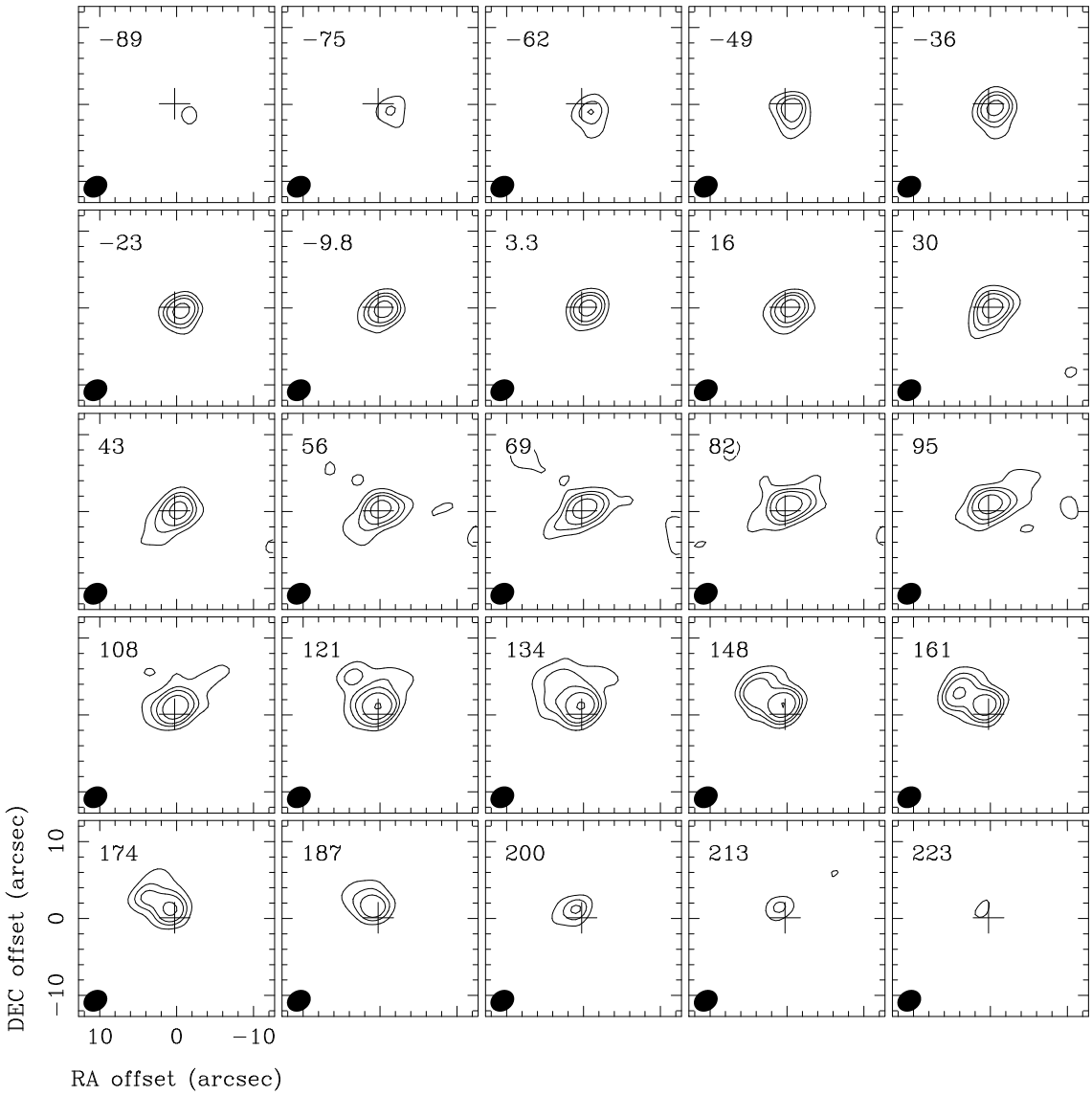

Fig. 6. Channel maps of the nuclear rotating molecular gas disc observed with the Plateau de Bure interferometer. The contours are 1, 2, 3, 5, 10, 15 × 0.01 Jy beam^{-1}. The central velocity is 2652 km s^{-1}.

Table 5. Parameters of ^{12}CO and ^{13}CO at the central position.

Line	Central velocity (lsr) (km s^{-1})		Linewidth (km s^{-1})		Peak (K)		int. Intensity (K km s^{-1})
^{12}CO(1–0)	2698	2796	125	147	0.02	0.036	7.52 ± 0.22
^{12}CO(2–1)	2655	2802	93	114	0.016,	0.039	6.10 ± 0.73
^{13}CO(1–0)	2725		208		0.0018		0.37 ± 0.06
^{13}CO(2–1)	2785		61		0.0033		0.25 ± 0.09

Gaussians were fitted to determine linewidths, peak intensity, and central velocity. For ^{12}CO, we fitted two components to the measured line, whereas for ^{13}CO only one component was fitted. The given intensity is integrated over both components. Temperatures are given in $T_{\rm MB}$.

4. Radiative transfer calculations

To investigate the physical conditions of the ISM, we used RADEX[4], which is a one-dimensional spherically symmetric non-LTE radiative transfer code available online (Schöier et al. 2005; van der Tak et al. 2007). In this code, the mean escape probability method for an isothermal and homogeneous medium is used in the calculations.

We assume that the ^{12}CO lines are optically thick ($\tau > 1$), so that the CO is self-shielded from the UV radiation field. The high ^{12}CO/^{13}CO line ratio limits the optical depths to $\tau < 10$, unless the ^{13}CO abundances are extraordinary low. Furthermore, we assume "standard" abundances of ^{12}CO and ^{13}CO of $X[^{12}\mathrm{CO}] = 10^{-4}$ and $X[^{13}\mathrm{CO}] = 2 \times 10^{-6}$, respectively (e.g., Blake et al. 1987; Mao et al. 2000). The line ratios fitted by the radiative transfer model constrain the average properties of an ensemble of clouds that do not fill the beam. We assume

[4] http://www.strw.leidenuniv.nl/~moldata/radex.html

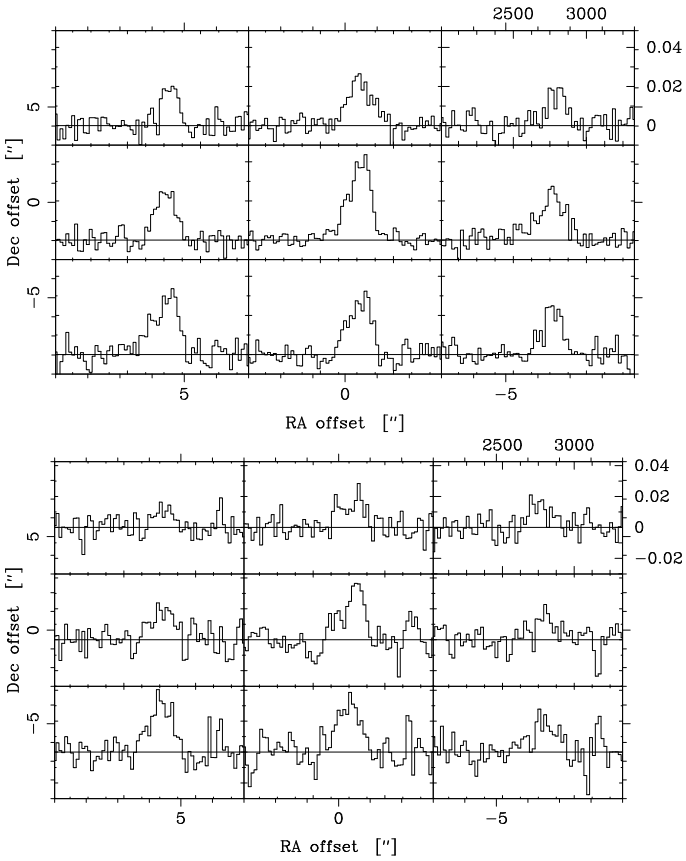

Fig. 7. Inner 6″ × 6″ of the CO map observed with the IRAM 30 m telescope. The outer tick marks denote the spacing of the observed positions, and the inner tick marks represent either the velocity (km s^{-1}) or $T_{\rm MB}$ (mK) (labeled in the upper right spectrum). *Top*: ^{12}CO(1−0) map of the central region. Note that the data are highly oversampled (beamsize 22″). *Bottom*: ^{12}CO(2−1) map of the central region. Note that the data are close to being fully sampled (beamsize 11″). See Figs. 3 and 4 for the larger-scale maps.

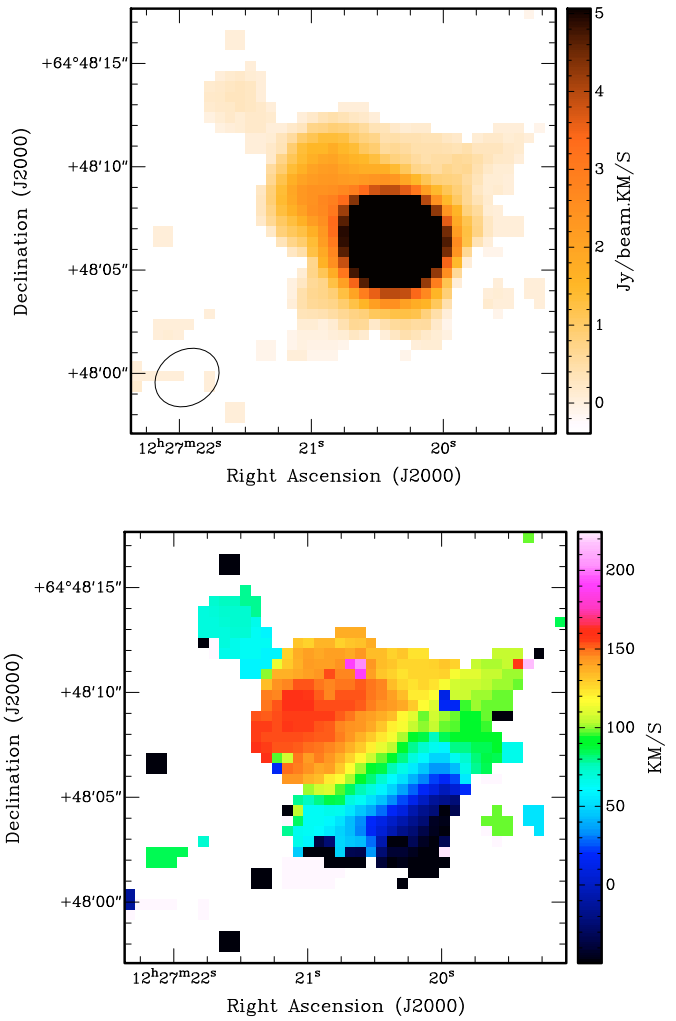

Fig. 8. Plateau de Bure maps of the central CO disc in NGC 4441: (*top*) the integrated intensity map, (*bottom*) the velocity map. The beam is shown in *the lower left corner of the upper panel*.

Table 6. Integrated intensity line ratios derived from the CO measurements at the central position.

Property	Result
$M_{\rm H2}$ (10^8 $M_\odot$)	4.6
^{12}CO(2–1)/^{12}CO(1–0)	0.5 (0.06)
^{13}CO(2–1)/^{13}CO(1–0)	0.42 (0.17)
^{12}CO(1–0)/^{13}CO(1–0)	21 (3.5)
^{12}CO(2–1)/^{13}CO(2–1)	25 (7.6)

In brackets, the errors in the line ratio are given, following standard error propagation calculations. A source size of 22″ is used to evaluate the line ratios.

that the emission emerges from a single cloud type, which is unlikely to be true, but provides us with a first measure of the main properties of the ^{12}CO/^{13}CO emitting gas.

We explore a range of H_2 column densities and temperatures of 10^{18}−10^{22} cm^{-2} and 10−50 K. In Fig. 12, the results for H_2 column densities of 10^{20} cm^{-2} and 10^{21} cm^{-2} are displayed. The levels decrease from high temperatures at low densities to low temperatures at high densities. The measured line ratios ^{12}CO(2−1)/^{12}CO(1−0) and ^{13}CO(2−1)/^{13}CO(1−0) are both indicative of subthermally excited emission, i.e., either low temperatures and/or low density.

The closest agreement between the models and both the ^{12}CO(2−1)/^{12}CO(1−0) and ^{13}CO(2−1)/^{13}CO(1−0) lines ratios is found for a column density per cloud of 10^{21} cm^{-2}.

From the ^{12}CO and ^{13}CO ratios alone, it is impossible to determine the temperature in a more specific way, but as seen in Fig. 12, for higher temperatures (>20 K) the density is well below 1000 cm^{-3}. There are no signs of warm, dense ($n > 10^4$ cm^{-3}) cores. For the gas to be dense yet still reproduce the observed line ratios, temperatures of 5 K are required, which is significantly lower than the dust temperature. This is of course technically possible, but this cold, dense component would quickly collapse and form stars. We find it more likely that the observed line ratios indicate a low density ($n <$ 1000 cm^{-3}) molecular ISM where the clouds are diffuse – i.e. not entirely self-gravitating – or consist of the extended outskirts of much smaller, bound clouds. This would be in agreement with the moderate to low star formation rate derived for NGC 4441 (Manthey et al. 2008a).

Interestingly, the ^{12}CO/^{13}CO line ratio in NGC 4441 is unusually high for a galaxy with a moderate to low star formation rate. Values found here are more reminiscent of starburst nuclei (15−20) (Aalto et al. 1995).

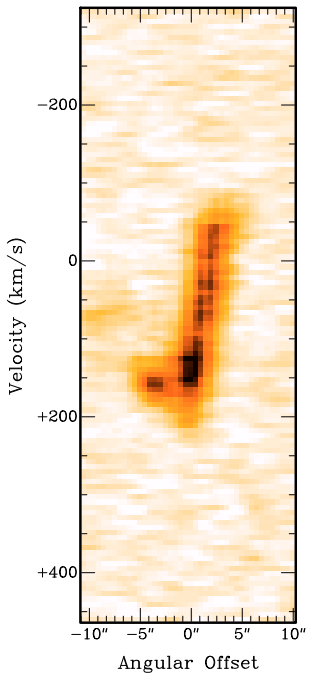

Fig. 9. *pv*-diagram along the major axis of the rotating CO disc. The position angle is PA = 222°, i.e., positive offsets are in the south-western direction. The central velocity is 2652 km s^{-1}.

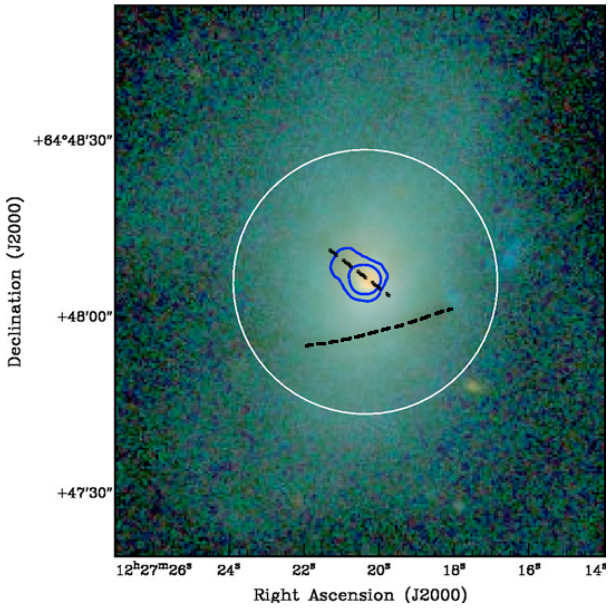

Fig. 10. SDSS *irg*-colour composite image of the main body of NGC 4441. Various dust lanes are visible. Overlaid are two contours of the CO distribution that highlight the extended and the compact component. The two dashed lines mark two dust lanes. Note that the central dust lane is associated with the molecular gas. This dust lane is broadend at the east side where a faint second peak in CO is seen. The white circle marks the primary beam of the Plateau de Bure interferometer.

It is possible that the ISM in NGC 4441 is the remnant of a burst of star formation that consumed the denser fraction of the gas. Diffuse gas may also reflect the dynamical impact of the merger on the gas properties: tidal forces, bar-induced shocks or the merger event.

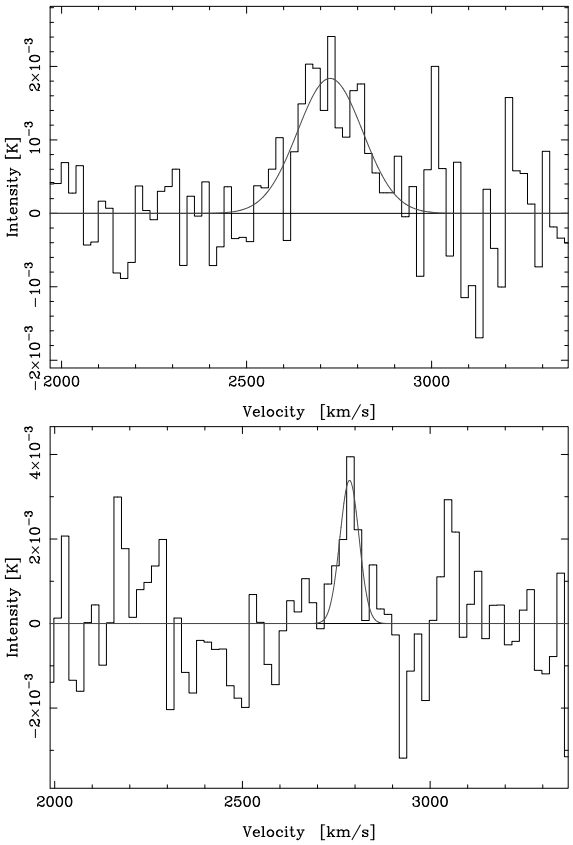

Fig. 11. ^{13}CO observed at the centre position of NGC 4441, measured with the IRAM 30 m telescope. The intensity is given in units of $T_{\rm MB}$. *Top*: $J = 1-0$, rms = 0.7 mK. *Bottom*: $J = 2-1$, rms = 1.3 mK. Overlaid are Gaussian fits to the lines. The parameters are given in Table 5.

5. Discussion

5.1. A counter-rotating nuclear molecular disc?

Nuclear rotating discs are often found in interacting galaxies (e.g., Bryant & Scoville 1996; Downes & Solomon 1998; Bryant & Scoville 1999; Yun & Hibbard 2001). Even though these studies concentrate on ULIRGs, some of the observed features are similar to the disc found in NGC 4441. The discs found in mergers of spirals are very compact, with typical radii of 300−800 pc. Furthermore, the molecular gas fraction traced by CO tends to have a rather low density (10^2−10^3 cm^{-3}) (Downes & Solomon 1998). Therefore, the CO lines are subthermally excited (Downes & Solomon 1998), as we also assume for NGC 4441. However, in ULIRGs turbulence is rather high (up to 100 km s^{-1}, e.g., Downes & Solomon 1998) which explains why gravitational instabilities occur leading to the observed high star formation rate. The ISM in the nuclear disc of NGC 4441 might be less turbulent due to a different merger history. If NGC 4441 is a S+E merger, only one partner brings in a significant amount of molecular gas to form an interaction-triggered disc more smoothly. Therefore, the disc might be more stable, and thus only moderate ongoing star formation is observed.

Besides the diffuse component generally found in ULIRGs, the bulk of the molecular gas is in a dense phase (10^5−10^6 cm^{-3}), as manifested by their extreme star formation (e.g., Solomon et al. 1992; Greve et al. 2009). Based on our radiative transfer modelling, we find no evidence of a dominant dense gas phase in NGC 4441, in agreement with its moderate star formation rate.

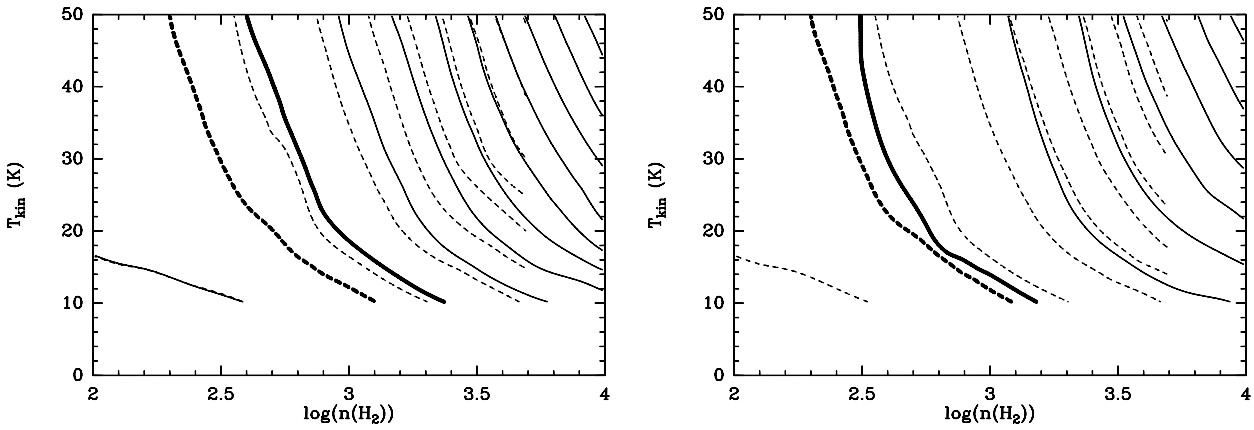

Fig. 12. Results of the RADEX analysis. The H_2 column density is 10^{20} cm^{-2} (*right*), and 10^{21} cm^{-2}. Shown are the line ratios of ^{12}CO(2−1)/^{12}CO(1−0) (solid) and ^{13}CO(2−1)/^{13}CO(1−0) (dashed). The bold lines mark the measured line ratios of NGC 4441. The levels of the line ratios start at 0.25 and proceed in steps of 0.25. For this analysis, we assumed a linewidth of 10 km s^{-1} per cloud and abundances of $X[^{12}\mathrm{CO}] = 10^{-4}$ and $X[^{13}\mathrm{CO}] = 2 \times 10^{-6}$.

Compared with the rotation of the large-scale HI disc (Manthey et al. 2008a), the nuclear molecular disc is kinematically decoupled. Its rotation axis is shifted by ∼100°.

Kinematically decoupled cores (KDCs) are found in various galaxies, in spirals as well as in S0 and ellipticals (e.g., Krajnović et al. 2008; Haynes et al. 2000; Kuijken et al. 1996). First simulations of Hernquist & Barnes (1991) showed that counter-rotating nuclear discs can occur in an equal-mass disc-disc merger in which the two progenitors have anti-parallel spins (i.e., a *retrograde* merger). In this scenario, the nuclear disc contains gas that originated in the centres of the original gas discs that was exposed to strong gravitational torques and thus lost most of the angular momentum. Because of that, no information about the original sense of rotation is preserved, and thus the rotation axis of the new disc is not related to those of the original progenitors. In contrast, the gas in the outer parts can retain its angular momentum and thus conserve the original motion. In this scenario, the merger remnants evolve into elliptical galaxies, which are often found to host a KDC.

Further theoretical studies showed that KDCs in S0 and spirals can be formed by minor mergers with gas-rich companions, and even mergers with at least one elliptical can lead to (stellar) KDCs (e.g., Bertola & Corsini 1999; Thakar & Ryden 1998; Haynes et al. 2000; di Matteo et al. 2008). Besides the variety of merging partners leading to a KDC, all simulations require that the merger geometry is retrograde.

5.1.1. Is the minor axis dust lane really an inclined disc?

The interpretation that the crossing central dust lane of NGC 4441 is an inclined disc seems likely because of the large velocity shift along the lane as well as the regular-looking shape of the associated *pv* diagram. The disc appears stable while hosting star formation and may contain diffuse, unbound molecular gas. However, one problem is the apparent counter-rotation of the inclined disc. In our previous paper on HI (Manthey et al. 2008a), we suggested that the interaction between the two galaxies was prograde, because of the large amount of angular momentum remaining in the gas of the tidal tails. However, retrograde mergers appear to be a requirement for producing counter-rotating cores. If the prograde scenario were correct, there would be a problem with the interpretation of the dust lane as an inclined disc. A final answer cannot be provided by these observations alone but would only be possible by comparing these results with numerical simulations.

Minor-axis dust lanes in other E+S mergers (such as Cen-A, Fornax-A, and NGC 4194 (the Medusa)) present a variety of dynamical behaviour. In the Medusa, the dust lane is morphologically similar to that in NGC 4441, but has a much smaller velocity gradient and is not interpreted as a disc, but rather as a lane along which gas is fed to the nucleus (Aalto & Hüttemeister 2000). In NGC 4441, however, we do not find evidence of such a central starburst.

5.2. Present state and expected future evolution of NGC 4441

The presence of an extended molecular gas reservoir in NGC 4441 is comparable to that found in NGC 4194, the prototypical S+E merger candidate (Aalto & Hüttemeister 2000). However, the relation between its geometry and optical appearance is different. In the Medusa, the CO roughly follows the direction of the optical tidal tail, whereas in NGC 4441 the molecular gas seems to be more extended towards the opposite side of the optical tail. This is probably caused by a different merger geometry of these two galaxies. In any case, extended molecular gas indicates that the merger history is different to that of ULIRGs in which molecular gas is concentrated in the central kpc. Based on their similar optical morphologies, particularly the strength of their tidal features, it seems likely that NGC 4441 and NGC 4194 are in similar merger states.

Interestingly, the molecular gas mass of NGC 4441 is only a quarter of that in the Medusa (4.6×10^8 $M_\odot$ for NGC 4441), whereas the amounts of atomic hydrogen are comparable (1.46×10^9 $M_\odot$ in NGC 4441 versus 2×10^9 $M_\odot$ in the Medusa, Manthey et al. 2008a,b). The question is, why has the starburst in NGC 4441 already faded, while the Medusa is still intensely forming stars. The relation between the ongoing star formation and the available resource for star formation (i.e., dense gas) can be expressed by the star formation efficiency: $\mathrm{SFE}\left(\frac{1}{\mathrm{yr}}\right) = \frac{SFR_{\mathrm{FIR}}}{M_{\mathrm{H2}}}$. Thus, for NGC 4441 we derive a star formation efficiency of SFE $= 2.1 \times 10^{-9}$ yr^{-1}. The equivalent gas depletion time is $\tau = 1/\mathrm{SFE} = 4.8 \times 10^8$ yr. If we assume a similar

conversion factor X_{CO} as that in the Medusa, we can directly compare the SFE with that in NGC 4194, because their metallicities are similar (Jütte et al. 2009, in prep.; Arimoto et al. 1996). Comparing NGC 4441 with the very effective starburst in the Medusa (of efficiency as high as 1.7×10^{-8} yr, Aalto & Hüttemeister 2000), NGC 4441 has a moderate star formation efficiency: SFE (NGC 4194) ~ 10 × SFE (NGC 4441). Since the H_2-to-CO conversion factor might be different for starbursting and "quiescent" galaxies, we may overestimate the mass, and therefore underestimate the SFE compared to the study of the Medusa. However, these dependencies are not yet well understood and cannot be taken into account here. From the radiative transfer models, we find that the molecular gas is rather thin and cold in NGC 4441, which makes it difficult to form new stars, whereas in the Medusa the CO lines are thermalised, indicating higher average gas densities and/or temperatures. It is, however, unclear, whether the differences are due to ageing effects, e.g., NGC 4441 might have transformed all the dense gas into stars, whereas in the Medusa this process is still ongoing. Furthermore, differences in the gas densities can be explained by the different gas reservoirs provided by the progenitors and/or the different merger geometries.

Thus, if this galaxy is already in a post-starburst phase, it still manages to retain a large amount of gas that remain in principle available for star formation.

This is in agreement with observations of so-called "E+A" galaxies, i.e., post-starburst with an optical spectrum, reflecting that of a strong A-star population superimposed on an old elliptical-like population. A small but significant fraction of E+A galaxies have optical tidal features, which are indicative of a merger event only 0.5−1 Gyr ago (e.g., Zabludoff et al. 1996; Blake et al. 2004). Furthermore, Buyle et al. (2006) obtained HI observations of a sample of E+A galaxies and showed that the total atomic gas content may not be consumed until a galaxy reaches its post-starburst phase.

Furthermore, a large amount of diffuse molecular gas can survive a starburst phase (Kohno et al. 2002), when the gas in the dense cores is consumed during the star formation process. It is argued by Kohno et al. (2002) that the remaining molecular gas can be stable to gravitational instabilities. These instabilities could lead to a condensation and thus trigger star formation. In particular in early-type galaxies such as NGC 4441, the mass density increases steeply towards the centre, producing a rise in the rotation velocity. Therefore, the epicyclic frequency, which is proportional to the critical mass density, also rises in addition to the critical mass density, which is the lower threshold density for possible star formation. In other words, the star formation is suppressed, although its raw material remains in the galaxy.

The small, regularly rotating, central molecular gas feature that is likely a disc seems to be stable, i.e., not star-forming, and is thus is similar to that found in NGC 5195 by Kohno et al. (2002).

6. Summary

We have obtained ^{12}CO(1–0) and (2–1) as well as ^{13}CO(1−0) and (2−1) observations of the advanced merger NGC 4441. The main results of this investigation are:

1. We observed the advanced merger remnant NGC 4441 in ^{12}CO(1−0) using the Onsala 20 m telescope. We determined a total molecular gas mass of 4.6×10^8 $M_\odot$.
2. The star formation efficiency was measured to be 2.1×10^{-9} yr^{-1} and the gas depletion time $\tau = 4.8 \times 10^8$ yr.
3. Following up, we mapped NGC 4441 with the single-dish IRAM 30 m telescope in ^{12}CO(1−0) and ^{12}CO(2−1). We found extended molecular gas out to 22″ (3.9 kpc).
4. Two distinct velocity components with a velocity difference of ~100 km s^{-1} were detected. The relative intensities of both components vary with both distance from the centre and with line transition.
5. High-resolution imaging using Plateau de Bure detected a small central rotating molecular gas disc hosting most of the molecular gas in NGC 4441. In contrast to ULIRGs, which also have a compact molecular gas disc that fuel their central superstarburst, the disc in NGC 4441 seems to be stable and thus does not support star formation.
6. The central molecular gas disc has a different sense of rotation than the large-scale H I distribution. This is a strong indicator of a kinematically decoupled core.
7. Furthermore, we observed the ^{13}CO(1–0) and ^{13}CO(2−1) line with the IRAM 30 m telescope to estimate the molecular gas properties using the radiative transfer model `RADEX`. We derived ^{12}CO(2−1)/^{12}CO(1−0) and ^{13}CO(2−1)/^{13}CO(1−0) line ratios that are consistent with a diffuse ($n_{H2} \leq 1000$ cm^{-3}) molecular medium. However, the ^{12}CO(1−0)/^{13}CO(1−0) ratio is unusually high (^{12}CO(1−0)/^{13}CO(1−0) = 21), which is typical of that of the inner centres of luminous starbursts (Aalto et al. 1995).
8. The moderate star-formation rate of 1−2 $M_\odot$ yr^{-1} is in good agreement with the results from the molecular gas analysis. Because not much dense ($n \geq 10^4$ cm^{-3}) gas is present, no enhanced ongoing star formation can occur. However, the strength of a past starburst remains unclear.
9. NGC 4441 may be a local candidate for an E+A galaxy, still hosting a significant amount of gas but the starbust has already faded.

Acknowledgements. We thank Evert Olsson for his assistance of the IRAM observations. We thank the Onsala Space Observatory, and IRAM staff for their support during the observations. This research has made use of the NASA/IPAC Extragalactic Database (NED) which is operated by the Jet Propulsion Laboratory, California Institute of Technology, under contract with the National Aeronautics and Space Administration. The research was partially supported by the German Science Organisation (DFG) through the Graduiertenkolleg 787.

References

Aalto, S., & Hüttemeister, S. 2000, A&A, 362, 42
Aalto, S., Booth, R. S., Black, J. H., & Johansson, L. E. B. 1995, A&A, 300, 369
Aalto, S., Hüttemeister, S., & Polatidis, A. G. 2001, A&A, 372, L29
Arimoto, N., Sofue, Y., & Tsujimoto, T. 1996, PASJ, 48, 275
Bergvall, N. 1981, A&A, 97, 302
Bertola, F., & Corsini, E. M. 1999, in Galaxy Interactions at Low and High Redshift, ed. J. E. Barnes, & D. B. Sanders, IAU Symp., 186, 149
Blake, G. A., Sutton, E. C., Masson, C. R., & Phillips, T. G. 1987, ApJ, 315, 621
Blake, C., Pracy, M. B., Couch, W. J., et al. 2004, MNRAS, 355, 713
Braine, J., & Combes, F. 1992, A&A, 264, 433
Braine, J., & Combes, F. 1993, A&A, 269, 7
Bryant, P. M., & Scoville, N. Z. 1996, ApJ, 457, 678
Bryant, P. M., & Scoville, N. Z. 1999, AJ, 117, 2632
Buyle, P., Michielsen, D., De Rijcke, S., et al. 2006, ApJ, 649, 163
de Vaucouleurs, G., de Vaucouleurs, A., Corwin, H. G., et al. 1995, VizieR Online Data Catalog, 7155, 0
di Matteo, P., Combes, F., Melchior, A.-L., & Semelin, B. 2008, A&A, 477, 437
Downes, D., & Solomon, P. M. 1998, ApJ, 507, 615
Dupraz, C., & Combes, F. 1985, Lecture Notes in Physics (Berlin: Springer Verlag), 232, 151
Greve, T. R., Papadopoulos, P. P., Gao, Y., & Radford, S. J. E. 2009, ApJ, 692, 1432
Haynes, M. P., Jore, K. P., Barrett, E. A., Broeils, A. H., & Murray, B. M. 2000, AJ, 120, 703

Hernquist, L., & Barnes, J. E. 1991, Nature, 354, 210
Horellou, C., & Booth, R. 1997, A&AS, 126, 3
Khochfar, S., & Burkert, A. 2003, ApJ, 597, L117
Kohno, K., Tosaki, T., Matsushita, S., et al. 2002, PASJ, 54, 541
Kojima, M., & Noguchi, M. 1997, ApJ, 481, 132
Krajnović, D., Bacon, R., Cappellari, M., et al. 2008, MNRAS, 390, 93
Kuijken, K., Fisher, D., & Merrifield, M. R. 1996, MNRAS, 283, 543
Manthey, E., Hüttemeister, S., Haberzettl, L., & Aalto, S. 2005, in The Evolution of Starbursts, ed. S. Hüttmeister, E. Manthey, D. Bomans, & K. Weis, AIP Conf. Proc., 783, 343
Manthey, E., Aalto, S., Hüttemeister, S., & Oosterloo, T. A. 2008a, A&A, 484, 693
Manthey, E., Hüttemeister, S., Aalto, S., Horellou, C., & Bjerkeli, P. 2008b, A&A, 490, 975
Mao, R. Q., Henkel, C., Schulz, A., et al. 2000, A&A, 358, 433
Naab, T., & Burkert, A. 2000, in Dynamics of Galaxies: from the Early Universe to the Present, ed. F. Combes, G. A. Mamon, & V. Charmandaris, ASP Conf. Ser., 197, 267
Naab, T., & Burkert, A. 2001, in Galaxy Disks and Disk Galaxies, ed. J. G. Funes, & E. M. Corsini, ASP Conf. Ser., 230, 453
Naab, T., Jesseit, R., & Burkert, A. 2006, MNRAS, 372, 839
Quinn, P. J. 1984, ApJ, 279, 596
Sanders, D. B., & Mirabel, I. F. 1996, ARA&A, 34, 749
Schöier, F. L., van der Tak, F. F. S., van Dishoeck, E. F., & Black, J. H. 2005, A&A, 432, 369
Solomon, P. M., Downes, D., & Radford, S. J. E. 1992, ApJ, 387, L55
Steinmetz, M. 2003, Ap&SS, 284, 325
Strong, A. W., Bloemen, J. B. G. M., Dame, T. M., et al. 1988, A&A, 207, 1
Thakar, A. R., & Ryden, B. S. 1998, ApJ, 506, 93
van der Tak, F. F. S., Black, J. H., Schöier, F. L., Jansen, D. J., & van Dishoeck, E. F. 2007, A&A, 468, 627
Weil, M. L., & Hernquist, L. 1993, ApJ, 405, 142
Weistrop, D., Eggers, D., Hancock, M., et al. 2004, AJ, 127, 1360
Yun, M. S., & Hibbard, J. E. 2001, ApJ, 550, 104
Zabludoff, A. I., Zaritsky, D., Lin, H., et al. 1996, ApJ, 466, 104